Magnetic g tensors for the $^4I_{15/2}$ and $^4I_{13/2}$ states of $Er^{3+}:Y_2SiO_5$

Yongchen Sun*
Department of Physics, The University of South Dakota, Vermillion, South Dakota 57069, USA
and Department of Physics, Montana State University, Bozeman, Montana 59717, USA

Thomas Böttger†
Department of Physics, Montana State University, Bozeman, Montana 59717, USA
and Department of Physics, University of San Francisco, 2130 Fulton Street, San Francisco, California 94117, USA

C. W. Thiel‡ and R. L. Cone§
Department of Physics, Montana State University, Bozeman, Montana 59717, USA
(Received 29 July 2007; published 29 February 2008)

We present the complete Zeeman g tensors for the lowest-energy $^4I_{15/2}$ and $^4I_{13/2}$ states of Er^{3+} doped into Y_2SiO_5 for both crystallographic sites deduced from orientation-dependent optical Zeeman spectroscopy over three orthogonal crystal planes. From these data, principal axes of the g tensors were determined for each crystallographic site. Along axes with maximum values, the effective g factors are 14.65 (site 1) and 15.46 (site 2) for the ground state, and 12.97 (site 1) and 13.77 (site 2) for the excited state. To minimize optical decoherence and spectral diffusion in device applications and high resolution spectroscopy, special directions for applying an external magnetic field have been found for each site, for which the ground- and excited-state g factors are equal. Among those directions, choices are presented that also maximize the ground-state splittings for all four magnetically inequivalent sites, thus optimizing the prospects for freezing out electron spin fluctuations and reducing decoherence and spectral diffusion significantly.

DOI: 10.1103/PhysRevB.77.085124 PACS number(s): 76.30.Kg, 71.70.Ej, 42.70.−a, 42.62.Fi

I. INTRODUCTION

Erbium-doped optical materials, including Y_2SiO_5 that is studied here, have attracted considerable attention for spatial-spectral holography,[1,2] quantum memory, and quantum computing applications[3–7] due to their long optical decoherence times T_2 of up to 4 ms.[8,9] This coherence time corresponds to a homogeneous linewidth of 73 Hz for $Er^{3+}:Y_2SiO_5$ at 1.5 K and 7 T, the narrowest linewidth measured for an optical transition in any solid.[10] These Er^{3+} transitions have the further advantage of falling in the 1.5 μm spectral range where highly developed optical communication components make applications particularly practical.

The excitement about applications in spatial-spectral holography, quantum computing, and quantum memories arises from the capabilities of these resonant optical materials for optical signal processing speeds of tens to hundreds of gigahertz, extremely long optical coherence storage times, very selective addressing of ions with the available ultrahigh spectral resolution, and all-optical storage at high spatial density, for example, in buffer memories. The narrow homogeneous optical linewidth associated with a subgroup of ions allows the material to process or store many parallel channels of data across the inhomogeneous line, with a rough figure of merit being the ratio of the inhomogeneous linewidth to the homogeneous linewidth that can be as large as $\Gamma_{inh}/\Gamma_h = 10^6 - 10^8$. The inhomogeneous linewidth also establishes the signal processing bandwidth, which can be 20–30 GHz in $Er^{3+}:Y_2SiO_5$ codoped with magnetically inert Eu^{3+} to produce additional application-tailored inhomogeneous broadening, which can be several hundred gigahertz in $Er^{3+}:LiNbO_3$,[11] glasses,[12] and optical fibers.[13]

To realize the full potential of this material in spatial-spectral holography and quantum memory applications, the complete g tensors in both the ground and excited states for both crystallographic sites are needed to minimize decoherence effects due to spectral diffusion. Decoherence arises from magnetic dipole-dipole interactions with fluctuating magnetic moments of neighboring Er^{3+} ions in their ground states, a detailed study of which we recently reported with experimental measurements of spectral diffusion by stimulated photon echoes and modeling of the spin dynamics.[9,14] There are two goals one wants to achieve when selecting a direction to apply a magnetic field: (1) to reduce interactions between the optically active ion and the environmental spin systems, and (2) to reduce the entropy of the spin systems. Choosing directions where the ground-state and excited-state Zeeman g factors are equal reduces the Er^{3+} ion's sensitivity to these magnetic fluctuations and addresses the first goal. To achieve the second goal, one should apply an external magnetic field to freeze out populations of the magnetic excitations themselves. This can be accomplished by choosing directions where all Er^{3+} ions have large g factors in their ground states. As we shall show, it is possible to choose both equal g factors and large ground-state g factors under several practical conditions.

In this work, we are seeking a different regime of coherence control where spectral diffusion is significantly reduced. Part of the information required to analyze field directions has been reported in the literature. General optical spectroscopy of the material, including limited measurements of the Zeeman effect, has been reported earlier.[15] Ground-state g-factor measurements were made by Kurkin and Chernov using electron paramagnetic resonance (EPR) in a crystal that had a "poorly marked" cleavage plane containing the b

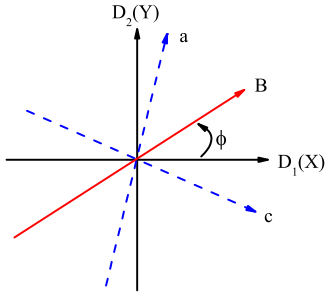

FIG. 1. (Color online) Sense of rotation adopted for the magnetic field B in the D_1-D_2 plane. The b axis points out of the page. Note that clockwise and counterclockwise rotations are not equivalent for this case.

axis.[16] Along the direction normal to this cleavage plane, they found $g=9.0\pm1.5$ for what they labeled site I, and $g=4.5\pm0.6$ for site II. Note that Kurkin and Chernov's site I (site II) corresponds to site 2 (site 1) common in the optics literature[8,15] and this paper. They also determined that the maximum values of the g factors were 15.465 and 14.804 along directions that form $57\pm3°$ and $73\pm3°$ angles with the normal direction of the cleavage plane for site I and site II, respectively. Since no other information regarding the crystal orientation was reported, the g factors for arbitrary orientations cannot be determined. More recently, Guillot-Noël *et al.*[17] published the g tensors and the quadrupole hyperfine parameters for the ground state of both sites, but the excited states were not studied.

In this paper, we report our measurement by high-resolution laser absorption of orientation-dependent Zeeman splittings for the $^4I_{15/2}(1)\leftrightarrow{}^4I_{13/2}(1)$ transition in $Er^{3+}:Y_2SiO_5$. Measurements were carried out in three independent planes of the crystal, allowing the full g tensors of both the ground and excited states for each crystallographic site to be determined. Those results then allow us to determine the special directions for applying an external magnetic field for freezing out electron spin fluctuations and reducing magnetic ion-ion interactions that lead to decoherence.

II. CRYSTAL STRUCTURE AND SYMMETRY CONSIDERATIONS

The Y_2SiO_5 crystal has the space group C_{2h}^6 with the C_2 axis labeled as b, and the a and c axes located in the mirror plane that is perpendicular to the b axis. The lattice constants are $a=1.041$ nm, $b=0.6721$ nm, and $c=1.249$ nm, and $\beta=102°39'$ is the angle between the a and c axes. The convention of Maksimov *et al.*[18] was used in labeling the crystal axes, and those of Li *et al.*[19] in labeling the optical extinction axes D_1 and D_2. For describing the g tensors, D_1, D_2, and b were used as X, Y, and Z in a right-handed coordinate system. The directions D_1 and D_2 used as coordinate labels in the experiments were determined by viewing the crystal between crossed polarizers, and the a and c axes were determined by Laue x-ray diffraction; D_1 is 23.8° from the c axis and 78.7° from the a axis, and D_2 is perpendicular to D_1 as shown in Fig. 1. The relationship between the two sets of axes is important because clockwise and counterclockwise rotations about the C_2 axis are not equivalent.

In $Er^{3+}:Y_2SiO_5$, the Er^{3+} ions substitute for Y^{3+} ions that occupy two distinct crystallographic sites, each with C_1 local symmetry. For each crystallographic site, there are four subclasses of sites with different orientations, related by the C_2 rotation and by inversion. These subclasses can be divided again into two groups. Those related by inversion interact identically with a magnetic field in an arbitrary direction, so they are always magnetically equivalent. Those related by a C_2 rotation interact differently with the magnetic field in an arbitrary direction and are, thus, magnetically inequivalent. In general, therefore, we expect to see two magnetically inequivalent subclasses of sites for each crystallographic site. For the special cases of a magnetic field along the b axis or in the D_1-D_2 plane, however, all of the subclasses of a given site become magnetically equivalent and this information can be used together with real time displays of the spectra to align the crystal with respect to the magnetic field. Related symmetry considerations regarding interaction of these sites with the optical electric field were reported earlier.[20]

III. EXPERIMENTAL METHODS

A 0.005% $Er^{3+}:Y_2SiO_5$ crystal of growth number 7-167 from Scientific Materials Corporation of Bozeman, Montana, was chosen for its narrow absorption lines so maximum spectral resolution can be achieved in the Zeeman experiments.[15] The Zeeman experiments were carried out in a vertical-access Oxford Spectromag cryostat with a horizontal magnetic field. The crystal was mounted in a custom sample holder that could rotate the crystal around an axis that is perpendicular to the applied magnetic field. The sample was rotated by a worm gear driven from the top of the cryostat by a vertical shaft, with the rotation angle determined from the known gear ratio. Alignment of the sample in the cryostat, especially when rotating about D_1 or D_2, was confirmed by using a telescope to view the sample relative to known reference lines in the field of view. Even though great care was taken, slight misalignment could not be avoided in the experiments; when the rotation axis was not exactly perpendicular to the magnetic field, the field direction rotated on a nearly flat conic surface rather than an ideal plane. These misalignment issues were addressed by the fitting procedures used in the data analysis as will be described later. Overall, we are confident that the axes were determined to within better than 1°.

The $^4I_{15/2}(1)\leftrightarrow{}^4I_{13/2}(1)$ transitions occur at 1536.478 nm (site 1) and 1538.903 nm (site 2) in vacuum. These values were calibrated against a $H^{13}C^{14}N$ gas cell frequency reference and are in agreement with Ref. 15, but supersede earlier published values that were measured in air.[8] High-resolution laser absorption spectra were recorded with a homemade external cavity diode laser (ECDL) capable of continuously scanning ~40 GHz. As described in Ref. 15, a high precision marker established by a heterodyne signal provided by a second ECDL with a manually adjustable frequency allowed each absorption frequency to be measured with a Burleigh wave meter to an absolute accuracy of ±20 MHz. By deter-

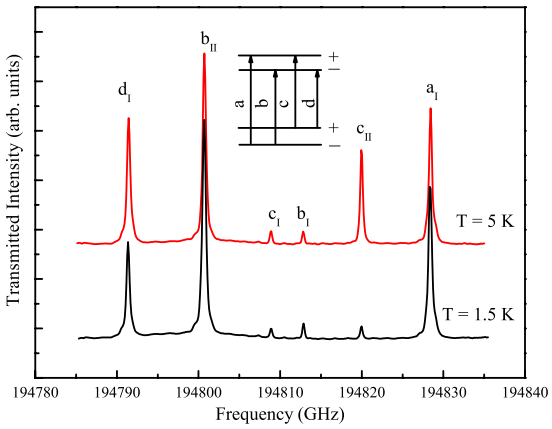

FIG. 2. (Color online) Zeeman laser absorption spectra for site 2 with $B=1$ T at $\theta=16.5°$ in the b-D_1 plane for $T=1.5$ K and $T=5$ K, showing thermal depopulation of the upper Zeeman components of the ground state in the lower temperature spectra; the two magnetic subclasses have been labeled with indices I and II, respectively. Transition labels are shown in the inset.

mining the frequency in this way, we completely avoided the nonlinearity associated with piezoelectric laser scans and also avoided possible laser drifts during the measurement.

IV. ZEEMAN RESULTS

The Er^{3+} ions have an odd number of electrons so that at zero field the energy levels are, at least, doubly degenerate from Kramers' theorem. Each zero field optical transition splits into four transitions in a field and, due to the magnetic site inequivalence discussed in Sec. II, there are eight transitions when the magnetic field is in an arbitrary direction. When the magnetic field is along the b axis or in the D_1-D_2 plane, the eight transitions for each crystallographic site merge into four.

Measuring the transition energies as the orientation of the magnetic field was varied allowed the g factors in both the ground and excited states to be determined for each plane. The ground and excited states each were regarded as isolated doublets, an assumption justified by observation of the linear Zeeman effect and by the energy level structure reported previously.[15] We follow the transition-labeling scheme of Ref. 15, using $(+)$ and $(-)$ to label the upper and lower Zeeman components of the ground and excited levels as shown in the inset of Fig. 2, and E_a for the transition energy of the ground-state $(-)$ component to the excited-state $(+)$ component, E_b for the $(--)$ transition, E_c for $(++)$, and E_d for the $(+-)$ transition. From the transition energies, the effective ground-state g factor is given by

$$g_g = (E_a - E_c)/\mu B = (E_b - E_d)/\mu B, \tag{1}$$

and the excited-state g factor is given by

$$g_e = (E_a - E_b)/\mu B = (E_c - E_d)/\mu B, \tag{2}$$

where μ is the Bohr magneton.

For the four absorption transitions of each site subclass in a Zeeman experiment, the assignment of the two outer transitions a and d can be verified easily because the highest-energy transition a always starts from the lower Zeeman component of the ground state and terminates on the upper Zeeman component of the excited state; similarly, the lowest-energy transition d always starts on the upper component of the ground state and terminates on the lower component of the excited state. The two inner transitions b and c, however, are not always easy to identify since either one can be higher in energy. To make confident assignments of the two inner transitions, extra temperature-dependent measurements were sometimes necessary. Transitions c and d, starting at the upper Zeeman component of the ground state, diminish in intensity at lower temperatures because of thermal depopulation of that component. Figure 2 illustrates this effect by plotting Zeeman absorption spectra for site 2 in a field of 1 T at 16.5° in the b-D_1 plane at two different temperatures. This figure shows only six of the eight transitions; the other two were outside the range of the plot. At 5 K, no distinction of the two inner transitions b and c was evident; however, by lowering the temperature to 1.5 K, the transitions labeled c_I, c_{II}, and d_I diminish in intensity and, thus, must originate from the upper component of the ground state, while the other transitions labeled a_I, b_I, and b_{II} must be from the lower component of the ground state. The subscript labels I and II here correspond to the different subclasses of site 2. Since the c_I and d_I transition intensities diminished by a similar amount relative to b_I and a_I enhancements, respectively, but by a much smaller amount compared to that of the c_{II} reduction or b_{II} enhancement, they were assigned to the same subclass. Since population of the upper components of the ground state is required for observing the c and d transitions, most of our experiments were carried out at 5 K, with other temperatures used as needed.

The orientation-dependent Zeeman spectra for three different planes for site 1 are plotted in Fig. 3. Angle ϕ is the azimuthal angle of the D_1-D_2-b coordinate system and is measured from D_1 in the D_1-D_2 plane. θ is the polar angle and is measured from b. The absorption linewidths were ~500 MHz at 5 K. Circles representing the data points are much larger than uncertainties in the measurements of the transition energy, but they do represent the scale of uncertainty in the angle measurements. As pointed out in Sec. II, the overall angular dependencies for clockwise and counterclockwise rotations are not equivalent in the D_1-D_2 plane. For that reason, the sense of rotation was defined explicitly in Fig. 1. The spectra in the other two planes are symmetric with respect to the major axes, as expected from the mirror symmetry plane (D_1-D_2) and the twofold rotation symmetry (around b).

Careful inspection of the data reveals a slight deviation from perfect symmetry, as evidenced by more than four allowed transitions detected at the 0 and 180° angles for the D_2-b plane spectra and the b-D_1 plane spectra. This arises from the slight crystal misalignment described earlier, which caused the magnetic field to map out a nearly flat conic surface rather than a plane. Simulations of the experimental data indicated by the solid lines in Fig. 3 show excellent agreement and are described in detail later in the paper.

Corresponding Zeeman data for site 2 are presented in Fig. 4, with the D_1-D_2 plane data in Fig. 4(a) showing C_2

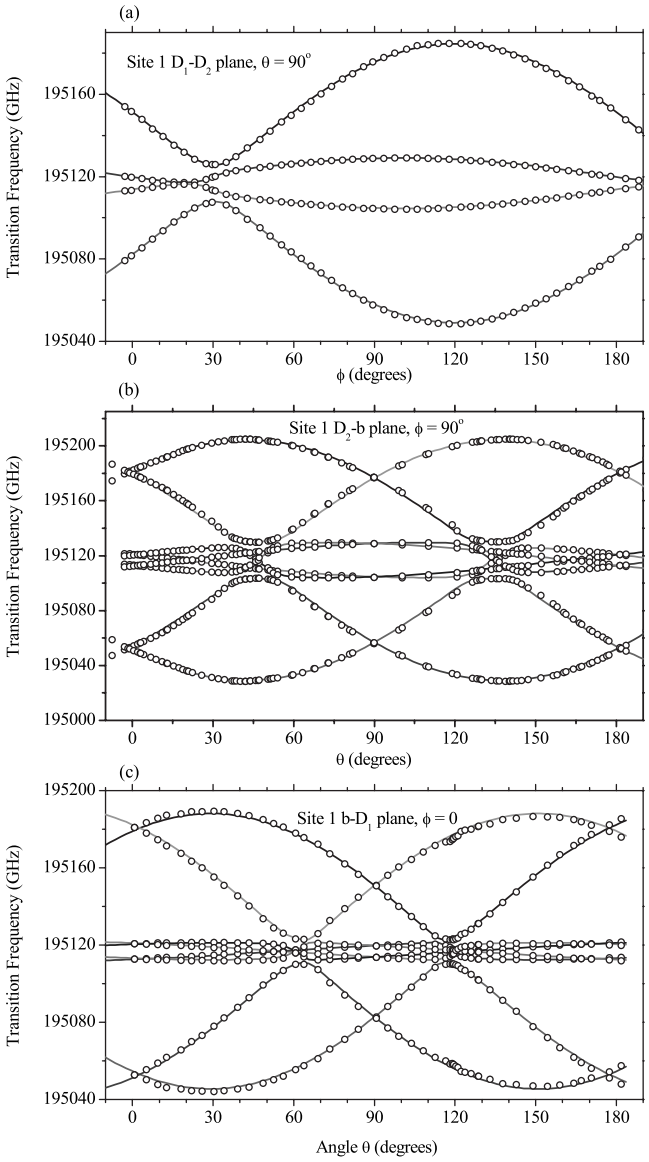

FIG. 3. Experimental Zeeman data for site 1 in three orthogonal planes taken in a field of 0.484 T. (a) shows the D_1-D_2 plane where the angle zero denotes the D_1 axis, (b) the D_2-b plane, and (c) the b-D_1 plane with angle zero denoting the b axis. In (c), the field maps out a slightly conic surface in the crystal. Line types are not coordinated for each site.

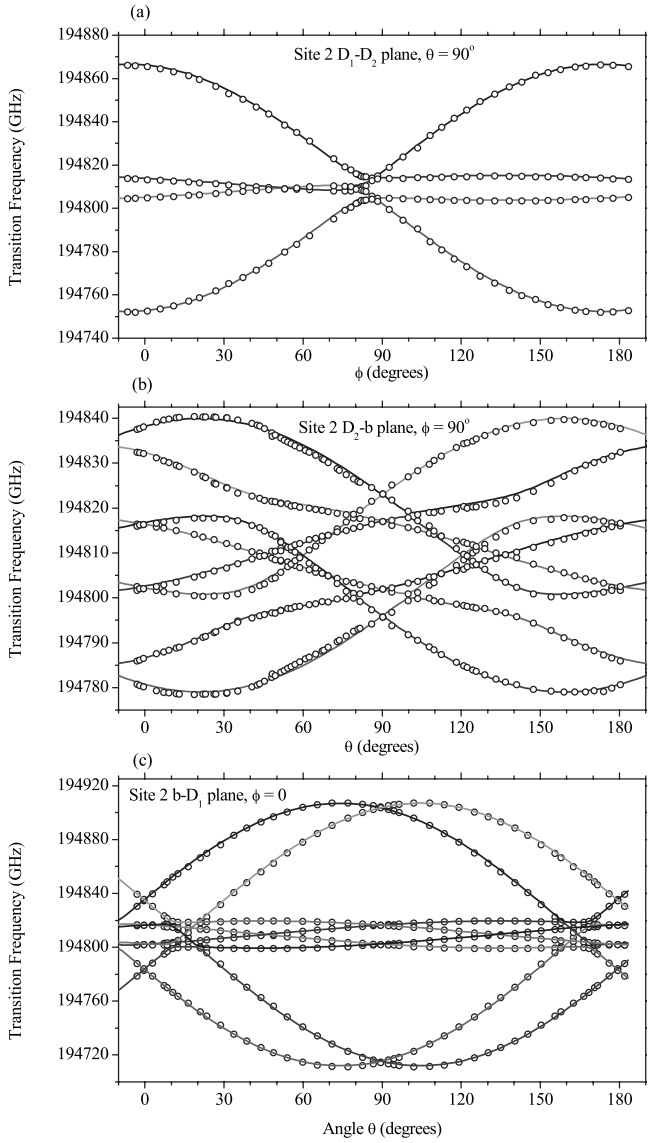

FIG. 4. Experimental Zeeman data for site 2 in three orthogonal planes. The D_1-D_2 data were taken in a field of 0.290 T due to larger g factors in that plane, and data from the other two planes were taken in a field of 0.484 T. Subplot designations and angle labeling conventions are the same as in Fig. 3. In (b), the field maps out a slightly conic surface in the crystal.

symmetry and the D_2-b and b-D_1 plane data in Figs. 4(b) and 4(c), respectively, showing mirror symmetry. The total splitting is much smaller in the D_2-b plane compared to those in the other two planes (note the scales and the different fields used); in addition, splittings are much larger for fields applied in the D_1 direction compared to fields applied in the D_2 direction. The eight transitions in the D_2-b plane data in Fig. 4(b) did not merge into four transitions as expected at 0 and 180°, as a consequence of the minor crystal misalignment discussed earlier.

The g factors for various orientations and for both sites were calculated from the data in Figs. 3 and 4 using Eqs. (1) and (2). Figure 5 displays the $^4I_{15/2}$ ground-state and $^4I_{13/2}$ excited-state g factors for site 1 for all three planes; solid symbols denote g factors for the ground state and open symbols denote those for the excited state. For convenience of discussion, the magnetic site subclasses are labeled as I and II. Figure 6 displays the corresponding data for site 2.

In extracting g tensors from the effective g factors over the three planes, a major challenge was the assignment of the correspondence between site subclasses in the D_2-b plane and the b-D_1 plane. Different combinations were applied in the fitting, and only one combination yielded reasonable results. Transition labels were assigned eventually to the site subclasses so that they are consistent in both planes, i.e., the subclass I (II) in the D_2-b plane and the subclass I (II) in the b-D_1 plane are the same subclass.

Only the absolute value of the principal g factors may be determined from the Zeeman experiments because of the

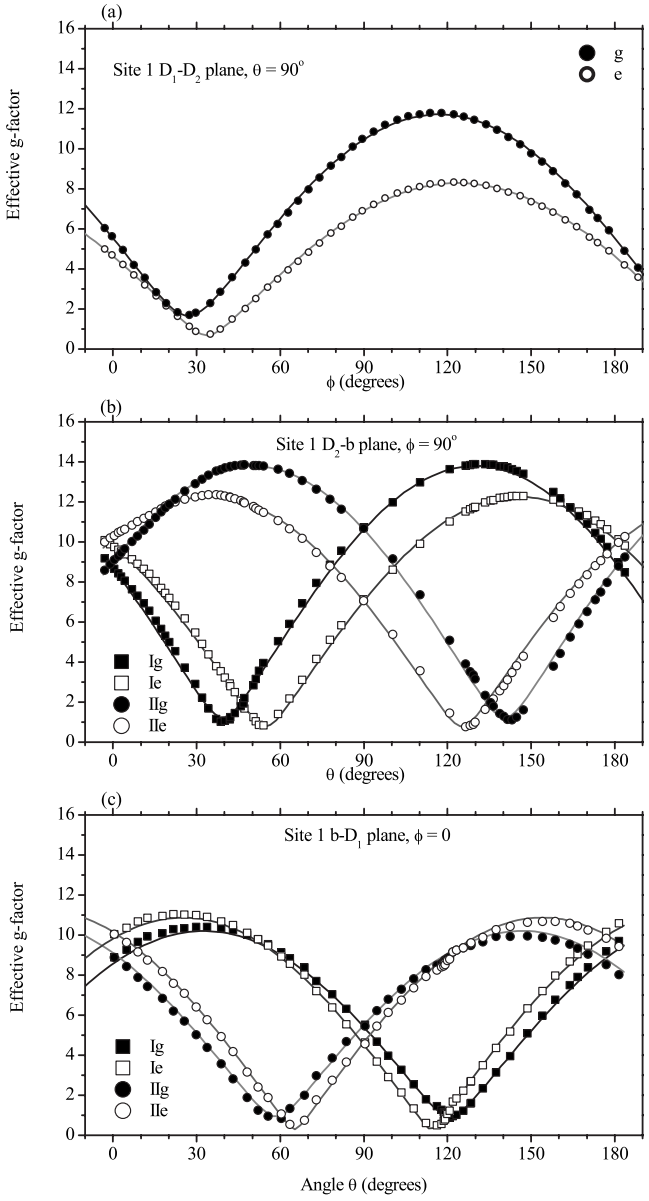

FIG. 5. Effective g-factor variations for site 1 in all three planes for the lowest-energy $^4I_{15/2}$ and $^4I_{13/2}$ states of $Er^{3+}:Y_2SiO_5$. Solid lines are least-squares fits to the data showing excellent agreement. Labels I and II are for magnetic subclasses; g and e for ground and excited states.

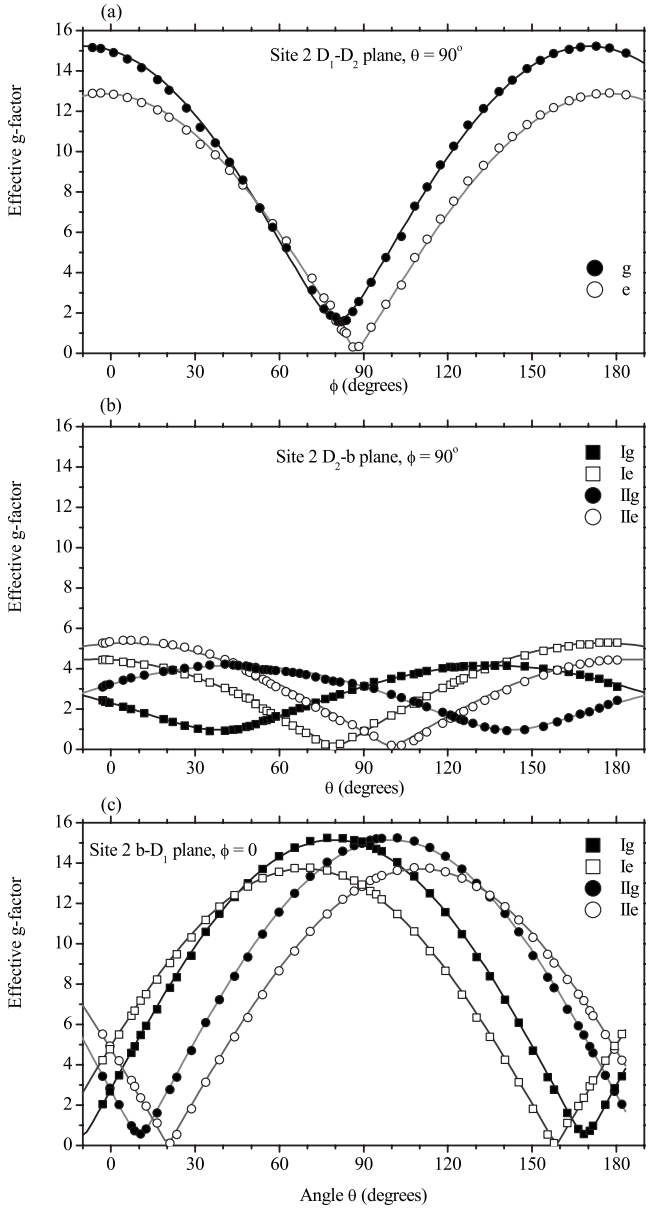

FIG. 6. Effective g-factor variations for site 2 in all three planes for the lowest-energy $^4I_{15/2}$ and $^4I_{13/2}$ states of $Er^{3+}:Y_2SiO_5$. Solid lines are least-squares fits to the data showing excellent agreement. Labels I and II are for magnetic subclasses; g and e for ground and excited states.

pseudovector character of the magnetic moment and the low site symmetries. Thus, there are eight possible matrices that could give the same Zeeman splitting patterns, and those matrices are related to each other by reversing the orientation of each principal axis. In this work, we chose one particular set of signs. This choice gives a complete description of the energy level splittings. It should be noted that this does not preclude use of other matrices. A complete crystal field analysis could possibly model transition intensities and, thus, aid the determination of relative signs, but the mixed electric and magnetic dipole contributions for the Er^{3+} $^4I_{15/2}(1) \leftrightarrow {}^4I_{13/2}(1)$ transition and the low site symmetry make such an analysis extremely difficult and well beyond the scope of the present paper.

A nonlinear least-squares fitting routine was applied to analyze the g-tensor data. To find the best overall fit, all five available sets of data were incorporated for each site, including one set from the D_1-D_2 plane where the subclasses were magnetically equivalent and two each from the D_2-b plane and b-D_1 plane where the subclasses were magnetically inequivalent. At the first stage of the analysis, all data were assumed to have been taken with the B field confined in the major planes so that misalignment issues were neglected initially. These results then were refined by considering the two possible misalignments: (1) the magnetic field does not lie in the plane of rotation so that the magnetic field maps out a

TABLE I. The g tensors for the $^4I_{15/2}(1)$ ground state and $^4I_{13/2}(1)$ excited state for both crystallographic sites with their magnetically inequivalent orientations I and II. The diagonal elements are the same for the two orientations that are related by C_2 symmetry. The off-diagonal elements are different but related as explained in the Appendix. The uncertainty of the parameters are listed in parentheses. As noted in the text, the data are in the D_1-D_2-b coordinate system.

				Orientation I			Orientation II		
	g_{xx}	g_{yy}	g_{zz}	g_{xy}	g_{zx}	g_{yz}	g_{xy}	g_{zx}	g_{yz}
Site 1									
Ground state	3.070(0.05)	8.156(0.04)	5.787(0.09)	−3.124(0.07)	3.396(0.081)	−5.756(0.052)	−3.124	−3.396	5.756
Excited state	1.950(0.24)	4.232(0.08)	7.888(0.07)	−2.212(0.12)	3.584(0.08)	−4.986(0.09)	−2.212	−3.584	4.986
Site 2									
Ground state	14.651(0.02)	1.965(0.04)	0.902(0.1)	−2.115(0.03)	2.552(0.03)	−0.550(0.05)	−2.115	−2.552	0.550
Excited state	12.032(0.10)	0.212(0.35)	1.771(0.67)	−0.582(0.10)	4.518(0.26)	−0.296(0.27)	−0.582	−4.518	0.296

conic surface, and (2) misalignment of the rotation axis relative to the major crystal axes. We take into account both issues by allowing the nominal D_2-b and b-D_1 surfaces actually probed to become conic and the rotation axes to deviate from the major axes in order to obtain the best fit in the presence of small crystal misalignments. It was found that the conic surfaces were all within 2° of a plane.

The full g tensors were determined relative to the coordinate system defined by $D_1(X)$, $D_2(Y)$, and $b(Z)$, and these axes were further defined relative to the crystal axes as shown in Fig. 1. The results for the ground and excited states of both site orientation subclasses for each crystallographic site are listed in Table I. The relative uncertainty in the determination of each value is also included in parentheses. Since the g tensors are symmetric, only six parameters are independent for each tensor. The g tensors of the two associated site subclasses are related by C_2 rotation of the space group, and, thus, only two of the six independent parameters reverse their signs. These are g_{xz} and g_{yz} as explained in the Appendix. The values of the g-tensor components were kept to three decimal places as listed in the table, since further truncation causes errors in the matrix calculations and in the orthogonality between the principal axes through the direction cosines.

By diagonalizing the g-tensor matrices, the principal values and the principal axes of each tensor were determined. The principal values, along with the direction cosines of the axes, are listed in Table II. The principal axes are labeled X, Y, and Z, and the directions have been chosen so that they form a right-handed coordinate system. It should be noted that the choice of the Z axis to correspond to the maximum g factor is arbitrary, as are the choices of the Y axis for the intermediate value and the X axis for the smallest value. The direction cosines (or Euler angles) describe how the local X'Y'Z' principal axis coordinate system of each ion is related to the crystal's XYZ coordinate system defined by the D_1-D_2-b axes.

In the determination of the principal values, the largest values are the most accurate, since their contributions to the data are larger; those values have uncertainties of 0.03, as determined from the covariance matrices of the fit. The greatest uncertainty occurred in determining the smallest principal value for the $^4I_{13/2}$ excited state for site 2. The small magnitude of that principal value means that its contributions to the measured effective g-factors are smaller than those of other principal values except in the very specific case when the field is applied precisely along that principal direction. The fit to the experimental data is consequently less sensitive to its value.

TABLE II. Principal values and g tensor coordinates of the ground– and excited-state g tensors. The l, m, and n values are direction cosines of the principal axes of the g-tensor in D_1-D_2-b coordinate system of the crystal. Only data for orientation I are listed here for both sites. The principal axes are labeled $X\prime$, $Y\prime$, and $Z\prime$, and the directions have been chosen so that they form a right-handed coordinate system with $Z\prime$ along the maximum g-factor direction.

		Ground state				Excited state			
		Principal g	l	m	n	Principal g	l	m	n
Site 1	$g_{z\prime}$	14.654(0.03)	0.3676	−0.7094	0.6013	12.974(0.02)	0.3565	−0.5293	0.7699
	$g_{y\prime}$	1.798(0.09)	0.6991	0.6372	0.3244	0.848(0.08)	0.3773	0.8354	0.3996
	$g_{x\prime}$	0.560(0.16)	0.6133	−0.3012	−0.7302	0.247 (0.21)	0.8547	−0.1481	−0.4975
Site 2	$g_{z\prime}$	15.461(0.02)	0.9713	−0.1594	0.1763	13.769(0.02)	0.9344	−0.0478	0.3530
	$g_{y\prime}$	1.636(0.05)	0.1799	0.9779	−0.1067	0.215(0.2)	0.1920	0.9023	−0.3859
	$g_{x\prime}$	0.420(0.1)	0.1554	−0.1354	−0.9785	0.031(0.2)	0.3001	−0.4283	−0.8523

TABLE III. Principal values for the different g tensors and the Euler angles (in degrees). The two orientations are related by a difference of 180° in the α values, while β and γ stay the same. The X'Y'Z' coordinate system is defined in Table II.

				Orientation I			Orientation II
	$g_{z'}$	$g_{y'}$	$g_{x'}$	α	β	γ	α
Site 1							
Ground state	14.654	1.798	0.560	−62.61	53.05	23.95	117.39
Excited state	12.974	0.848	0.247	−56.04	39.65	38.77	123.96
Site 2							
Ground state	15.461	1.636	0.420	−9.32	79.85	−6.22	170.68
Excited state	13.769	0.215	0.031	−2.95	69.37	−24.10	177.05

The corresponding Euler angle representations for the orientations of the g tensors relative to the crystal coordinate system are listed in Table III. A more detailed discussion of the application of the Euler angles in this context is given in the Appendix. More than one convention for the Euler angles can be found in the literature; that of Edmonds[21] is used here, and it is somewhat different from the convention recently used by Longdell *et al.*[22] for $Pr^{3+}:Y_2SiO_5$ or by Guillot-Noël *et al.* for this material.[17] Inspecting the Euler angles in Table III, we find that for site 1 the direction of the maximum value of the g tensor is defined by (0.3676, −0.7094, 0.6013) for the ground state and (0.3565, −0.5293, 0.7699) for the excited state. For site 2, these angles are (0.9713, −0.1594, 0.1763) for the ground state and (0.9344, −0.0478, 0.3530) for the excited state. Using these direction cosines, the directions for the maximum values differ by 14.2° (12.2°) between the ground and excited states for site 1 (site 2), a situation that is allowed for these low symmetry sites.

V. DISCUSSION

Comparing our maximum g-tensor values to those of Kurkin and Chernov,[16] it appears that their "site I" is our site 2. The labels are arbitrary, and this difference is not surprising as information for making the comparison was not available previously. Their measurements were all based on EPR, where a different transition-labeling scheme is used, while we have used labels consistent with Ref. 8, where the sites were arbitrarily labeled for optical transitions.

Our maximum g values closely match those of Kurkin and Chernov.[16] In the direction normal to the cleavage plane, Kurkin and Chernov found $g=9.0\pm1.5$ for their site I (our site 2) and 4.5 ± 0.6 for their site II (our site 1), and the corresponding directions for the maximum g factors form angles of $57\pm3°$ and $73\pm3°$, respectively, to the normal. Since the normal direction is perpendicular to the C_2 axis, it must be in the D_1-D_2 plane. Using their angles and the directions corresponding to our maximum g-tensor values, we find that their normal direction is at $\phi=48°$ in the D_1-D_2 plane. Comparing our results to the ground-state g tensor determined by Guillot-Noël *et al.*,[17] we see that they are very similar. The g factors along principal directions of the tensors are within 0.1 of each other with the exception of the smallest direction for site 1, where we have a value of 0.56 and they have 0.0. We should point out that both for our measurement and theirs, the spectra were not sensitive to the g factor along x since its magnitude is so small.

From the spin-lattice-relaxation experiments of Kurkin and Chernov,[16] the relaxation of site 1 (their site II) can be described by coupling to a 51 cm^{-1} level and that of site 2 (their site I) to a level at 58 cm^{-1}. A 63 cm^{-1} level was observed[15] for site 2 which is very compatible with those relaxation measurements, but there is no corresponding level for site 1. The closest level is at 40 cm^{-1} according to Ref. 15. We note here that the spin-lattice-relaxation experiments measure the relaxation rate from the coupling to all crystal field levels so that the discrepancy is not unexpected.

The effective g factors of these two states indicate that the ground-state wave function should primarily contain admixtures of the $|\pm\frac{15}{2}\rangle$, $|\pm\frac{13}{2}\rangle$, and $|\pm\frac{11}{2}\rangle$ states; the Lande g factor of this multiplet is about 1.20 independent of the admixtures. The lowest-energy $^4I_{13/2}$ state should primarily contain admixtures of the $|\pm\frac{13}{2}\rangle$ and $|\pm\frac{11}{2}\rangle$ states; the Lande g factor for that multiplet is about 1.11. If accurate crystal field calculations can be made in the future, admixture factors can be determined and compared to our g-tensor measurements.

To minimize decoherence, the ground-state and excited-state g factors should be the same for the active ion, and all the other Er^{3+} ions in the lattice should simultaneously have the largest ground-state g factors that can be achieved. For a field applied along one of those specific directions, the optically active ions are made insensitive to the perturbations induced by ground-state spin flips, and all sites have strong depopulation of the upper Zeeman component, thus minimizing ground-state spin flips. The large ground-state g factors are important since all sites, not just the site of the optically active ion, contribute to the decoherence through ground-state spin flips and subsequent changes in ion-ion interactions. An applied field generally gives rise to magnetically inequivalent sites, as discussed in Sec. II, so that also must be considered. For a device application, magnetic equivalency is desirable as it minimizes the overall doping concentration required for optical absorption, which in turn increases the overall Er^{3+}–Er^{3+} inter-ion distance and thereby reduces all ion-ion interactions.

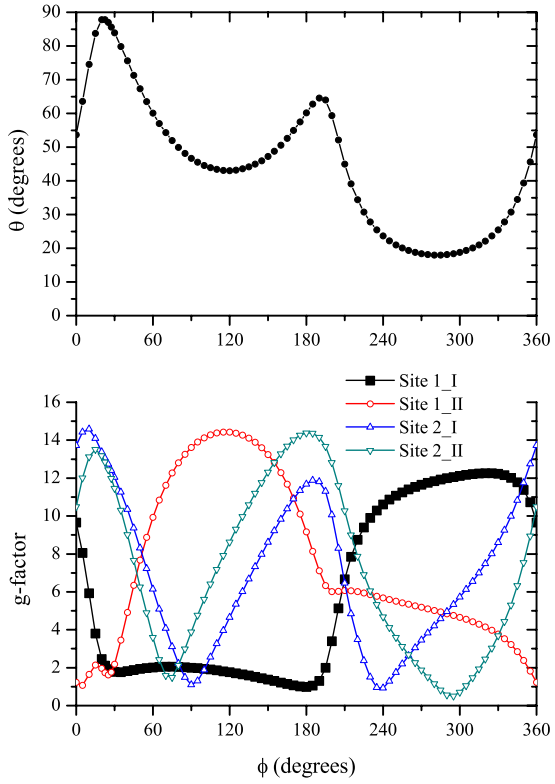

FIG. 7. (Color online) Calculated equal g-factor directions for subclass I of site 1 are shown in the upper plot. Those for subclass II can be determined from a C_2 rotation. In the bottom plot, all of the ground-state g factors are plotted for these directions.

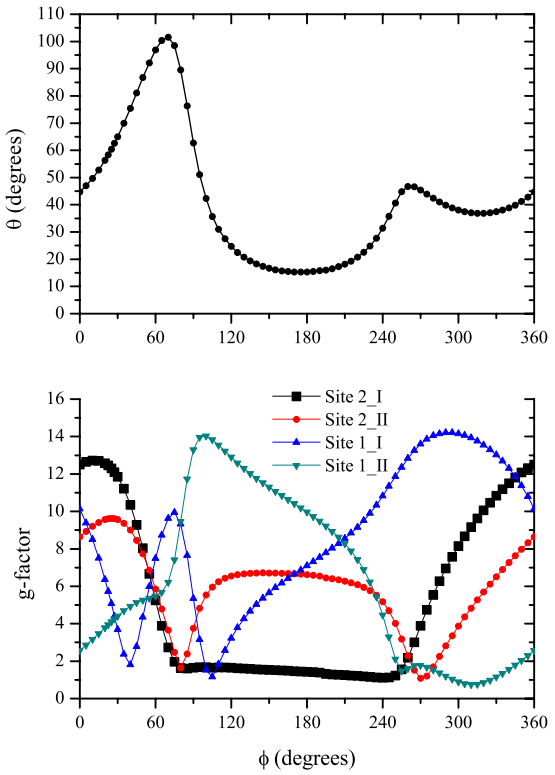

FIG. 8. (Color online) Calculated equal g-factor directions for subclass I of site 2. Those for subclass II can be determined from a C_2 rotation. In the bottom plot, all of the ground-state g factors are plotted for these directions.

Directions were calculated along which the excited state has the same g factor as the ground state. The results are presented in Fig. 7 for site 1 and in Fig. 8 for site 2. For each site, these directions make a closed trace as shown in the upper plots of both figures. For site 1, such special directions do not cross the D_1-D_2 plane at any time, and for site 2, there are two directions in the D_1-D_2 plane that satisfy the equal g-factor condition.

The following directions are proposed as starting points for finding the best coherence properties. For site 1, one initial candidate is

$$\phi = 209.6^\circ, \quad \theta = 45.0^\circ \quad \text{for subclass I}$$

$$\phi = 29.6^\circ, \quad \theta = 45.0^\circ \quad \text{for subclass II.}$$

For this direction, the active ion has g factors of 6.6 and the other ions have ground-state g factors of 6.0 (site 1 II), 6.6 (site 2 I), and 10.4 (site 2 II).

Another candidate is

$$\phi = 330.5^\circ, \quad \theta = 25.7^\circ \quad \text{for subclass I}$$

$$\phi = 150.5^\circ, \quad \theta = 25.7^\circ \quad \text{for subclass II,}$$

where the active ion has g factors of 12.2 and the other ions have ground-state g factors of 3.8 (site 1 II), 3.8 (site 2 II), and 8.7 (site 2 I).

For site 2, an initial candidate is

$$\phi = 0^\circ, \quad \theta = 44.7^\circ \quad \text{for subclass I}$$

$$\phi = 180^\circ, \quad \theta = 44.7^\circ \quad \text{for subclass II.}$$

The choice of ϕ here is made simply because it defines the b-D_1 plane, but ϕ probably could be varied by up to 30° (the corresponding θ changes as well) with similar degrees of optimization of the coherence properties. For this direction, the active ion has g factors of 12.5 and the other ions have g factors of 8.6 (site 2 II), 10.1 (site 1 I), and 2.6 (site 1 II).

The other two interesting directions for site 2 are in the D_1-D_2 plane as can be seen from the upper plot of Fig. 8. The first one is at

$$\phi = 53^\circ, \quad \theta = 90^\circ,$$

$$\phi = 233^\circ, \quad \theta = 90^\circ,$$

where g factors for the active ion are 7.2 and the ground state of site 1 has a g factor of 5.3. No subclass is labeled here since the two subclasses merge into one when B is in the D_1-D_2 plane. The second direction is at

$$\phi = 260^\circ, \quad \theta = 90^\circ,$$

$$\phi = 80^\circ, \quad \theta = 90^\circ,$$

where the active ion g factor is 1.66 and the site 1 ground-state g factor is 9.4.

An advantage of the D_1-D_2 plane choices is that the two site subclasses are magnetically equivalent. From consideration of the g-factor magnitudes, the first of these two directions seems to be preferred.

It should be emphasized that these directions are good starting points for finding the best direction to apply the field. They may not be the best directions. Other factors such as the operating temperature, ion number density affected by magnetic inequivalence, optical inhomogeneous linewidths, transition probabilities, and optical Rabi frequencies also may influence the choice of sites and field directions. For example, in the D_1-D_2 plane (θ=90°), for $120° < \phi < 150°$, the ground-state g factors for both crystallographic sites are at least 9.7, ensuring very efficient thermal depopulation of the upper Zeeman levels. Directions in that range should also be good candidates for long coherence times.

As a final note, we point out that a more sophisticated approach to reducing decoherence would minimize the magnetic dipole-dipole interaction directly, rather than just require that the ground- and excited-state g factors are equal. This is a challenging task due to the complexity of the dipole-dipole interaction in low symmetry systems such as Y_2SiO_5, and it is beyond the scope of the present work.

VI. SUMMARY

By determining the complete electronic g tensors and their orientations for both the $^4I_{15/2}(1)$ ground state and the $^4I_{13/2}(1)$ excited state in this low symmetry $Er^{3+}:Y_2SiO_5$ material, we have established conditions that should enable a different regime of control of the optical coherence of ions in solids, especially in systems containing odd-electron ions like Er^{3+}. This work enhances both the fundamental understanding of spectral diffusion and the potential performance of new devices requiring this material, including spatial-spectral holography, quantum memories, and quantum computing. As we have already measured the sharpest optical linewidths in $Er^{3+}:Y_2SiO_5$ observed for any solid, further improvements in the reduction or practical elimination of spectral diffusion may open the way for unprecedented material performance in these applications.

The work reported here establishes the path for making the general class of materials containing odd-electron ions and other paramagnetic ions completely competitive with the decoherence and spectral diffusion properties of the even-electron ions such as Pr^{3+}, Eu^{3+}, and Tm^{3+}. Until now, the primary efforts to demonstrate qubits and qubit manipulations have focused on those even-electron materials whose exceptionally weak paramagnetism almost eliminates spectral diffusion but whose transition wavelengths fall in spectral regions where custom modulators and other components are required to build prototype device systems.[23–32]

Our independently measured g tensor results for the ground state, obtained by high-resolution optical spectroscopy, were consistent with those determined by other groups using microwave EPR spectroscopy. The optical measurements also had comparable precision.

The ultranarrow linewidths observed for $Er^{3+}:Y_2SiO_5$ and other Er^{3+} materials[9,11,15] were unanticipated by many workers in the early days of high-resolution optical spectroscopy of solids, as it was thought that the paramagnetic interactions inevitably implied decoherence on a nanosecond scale. From that perspective, the developments reported here and the applications that they enable are particularly remarkable.

ACKNOWLEDGMENTS

This manuscript is based on research sponsored by the Air Force Research Laboratory under Agreement No. F49620-01-1-0313 and by the Montana Board of Research and Commercialization Technology. The views and conclusions contained herein are those of the authors only. The work of Y.S. is supported in part by the National Science Foundation/EPSCoR Grant No. 0091948 and by the State of South Dakota. T.B. wishes to acknowledge financial support through the University of San Francisco faculty development fund.

APPENDIX: EULER ANGLES

Our convention for the Euler angles followed that used by Edmonds.[21] We rotate the coordinate system and leave the physical property (vector, tensor, etc.) fixed in space. All rotations are counterclockwise. If the vector is described by $\mathbf{x}$ in the original coordinate system, it is described by $\mathbf{x}'$ in the new system and the vectors are related by

$$\mathbf{x}' = R\mathbf{x}, \tag{A1}$$

where R is the rotation matrix. For a tensor T, we have

$$T' = RTR^{-1} = RT\tilde{R}. \tag{A2}$$

We note here that this convention is different from the ones used in Refs. 17 and 22.

For a measured tensor given in Table I that is considered to be fixed in space, the coordinate system is rotated until the new coordinate system is aligned with the principal axes. After this rotation, in the new coordinate system, the tensor M' is

$$\begin{bmatrix} g_x & 0 & 0 \\ 0 & g_y & 0 \\ 0 & 0 & g_z \end{bmatrix} = R(\alpha,\beta,\gamma)MR^T(\alpha,\beta,\gamma), \tag{A3}$$

where g_x, g_y, and g_z are listed in Table II and the Euler angles are listed in Table III.

1. 180° rotation around the z axis

For a 180° rotation around the z axis, as in the relationship between the two site subclasses in Y_2SiO_5, the rotation matrix is given by

$$R = R^T = \begin{pmatrix} -1 & 0 & 0 \\ 0 & -1 & 0 \\ 0 & 0 & 1 \end{pmatrix}. \tag{A4}$$

After the rotation, the tensor is transformed as follows:

$$\begin{pmatrix} g_{xx} & g_{xy} & g_{xz} \\ g_{yx} & g_{yy} & g_{yz} \\ g_{zx} & g_{zy} & g_{zz} \end{pmatrix} \rightarrow \begin{pmatrix} g_{xx} & g_{xy} & -g_{xz} \\ g_{yx} & g_{yy} & -g_{yz} \\ -g_{zx} & -g_{zy} & g_{zz} \end{pmatrix}. \quad \text{(A5)}$$

Notice that the above transformation [Eq. (A5)] relates the tensor elements for site subclasses I and II shown in Table I.

2. Inversions

The inversion operation does not change a symmetric tensor. Thus, there are only two tensors related by the C_2 rotation for each crystallographic site.

*ycsun@usd.edu
†tbottger@usfca.edu
‡thiel@physics.montana.edu
§cone@montana.edu

[1] Z. Cole, Thomas Böttger, R. K. Mohan, R. Reibel, W. R. Babbitt, R. L. Cone, and K. D. Merkel, Appl. Phys. Lett. **81**, 3525 (2002).
[2] T. L. Harris, Y. Sun, R. L. Cone, R. M. Macfarlane, and R. W. Equall, Opt. Lett. **23**, 636 (1998).
[3] F. de Seze, A. Louchet, V. Crozatier, I. Lorgeré, F. Bretenaker, J.-L. Le Gouët, O. Guillot-Noël, and Ph. Goldner, Phys. Rev. B **73**, 085112 (2006).
[4] F. de Seze, A. Louchet, V. Crozatier, I. Lorgeré, F. Bretenaker, J.-L. Le Gouët, O. Guillot-Noël, and Ph. Goldner, J. Lumin. **121-123**, 526 (2007).
[5] M. U. Staudt, S. R. Hastings-Simon, M. Afzelius, D. Jaccard, W. Tittel, and N. Gisin, Opt. Commun. **266**, 720 (2006).
[6] M. U. Staudt, S. R. Hastings-Simon, M. Nilsson, M. Afzelius, V. Scarani, R. Ricken, H. Suche, W. Sohler, W. Tittel, and N. Gisin, Phys. Rev. Lett. **98**, 113601 (2007).
[7] S. Bertaina, S. Gambarelli, A. Tkachuk, I. N. Kurkin, B. Malkin, A. Stepanov, and B. Barbara, Nat. Nanotechnol. **2**, 39 (2007).
[8] R. M. Macfarlane, T. L. Harris, Y. Sun, R. L. Cone, and R. W. Equall, Opt. Lett. **22**, 871 (1997).
[9] Thomas Böttger, C. W. Thiel, Y. Sun, and R. L. Cone, Phys. Rev. B **73**, 075101 (2006a).
[10] Thomas Böttger, Y. Sun, C. W. Thiel, and R. L. Cone, Proc. SPIE **4988**, 51 (2003).
[11] Y. Sun, in *Spectroscopic Properties of Rare Earths in Optical Materials*, edited by G. Liu and B. Jacquier (Springer-Verlag, Berlin, 2005), Chap. 7, pp. 379–429.
[12] Y. Sun, R. L. Cone, L. Bigot, and B. Jacquier, Opt. Lett. **31**, 3453 (2006).
[13] R. M. Macfarlane, Y. Sun, P. B. Sellin, and R. L. Cone, Phys. Rev. Lett. **96**, 033602 (2006).
[14] T. Böttger, Ph.D. thesis, Montana State University-Bozeman, 2002.
[15] Thomas Böttger, C. W. Thiel, Y. Sun, and R. L. Cone, Phys. Rev. B **74**, 075107 (2006).
[16] I. N. Kurkin and K. P. Chernov, Physica B & C **101**, 233 (1980).
[17] O. Guillot-Noël, Ph. Goldner, Y. L. Du, E. Baldit, P. Monnier, and K. Bencheikh, Phys. Rev. B **74**, 214409 (2006).
[18] B. A. Maksimov, V. V. Ilyukhin, Y. A. Kharitonov, and N. V. Belov, Kristallografiya **15**, 926 (1970).
[19] C. Li, C. Wyon, and R. Moncorgé, IEEE J. Quantum Electron. **28**, 3 (1992).
[20] Y. Sun, G. M. Wang, R. L. Cone, R. W. Equall, and M. J. M. Leask, Phys. Rev. B **62**, 15443 (2000).
[21] A. R. Edmonds, *Angular Momentum in Quantum Mechanics* (Princeton University Press, Princeton, NJ, 1985).
[22] J. J. Longdell, M. J. Sellars, and N. B. Manson, Phys. Rev. B **66**, 035101 (2002).
[23] J. J. Longdell, M. J. Sellars, and N. B. Manson, Phys. Rev. Lett. **93**, 130503 (2004).
[24] J. J. Longdell and M. J. Sellars, Phys. Rev. A **69**, 032307 (2004).
[25] E. Fraval, M. J. Sellars, and J. J. Longdell, Phys. Rev. Lett. **95**, 030506 (2005).
[26] N. Ohlsson, R. K. Mohan, and S. Kröll, Opt. Commun. **201**, 71 (2002).
[27] M. Nilsson and S. Kröll, Opt. Commun. **247**, 393 (2005).
[28] L. Rippe, M. Nilsson, S. Kröll, R. Klieber, and D. Suter, Phys. Rev. A **71**, 062328 (2005).
[29] B. Kraus, W. Tittel, N. Gisin, M. Nilsson, S. Kröll, and J. I. Cirac, Phys. Rev. A **73**, 020302(R) (2006).
[30] J. H. Wesenberg, K. Mølmer, L. Rippe, and S. Kröll, Phys. Rev. A **75**, 012304 (2007).
[31] M. S. Shahriar, P. R. Hemmer, S. Lloyd, P. S. Bhatia, and A. E. Craig, Phys. Rev. A **66**, 032301 (2002).
[32] M. D. Lukin and P. R. Hemmer, Phys. Rev. Lett. **84**, 2818 (2000).